# Model-Based Static Compliance Analysis and Control for Pneumatic-Driven Soft Robots

Jialei Shi, Sara-Adela Abad, *Member, IEEE*, Ge Shi, *Member, IEEE*, Wenlong Gaozhang, *Student Member, IEEE*, Jian Sheng Dai, *Fellow, IEEE*, and Helge A. Wurdemann, *Member, IEEE*

***Abstract*—Elastomer-based soft manipulators have been explored in various fields due to their inherent compliant properties. Understanding and regulation of robot's compliance are important to the design, modeling, and control of soft robots. However, the elastomers are nonlinear hyperelastic materials with distributed compliance. This property makes the compliance modeling and control of soft robots fundamentally different and more complex from their rigid counterparts. This article presents a neo-Hookean model-based compliance modeling and control approach to investigate and regulate the configuration-dependent compliance property of a pneumatic-driven soft manipulator. The neo-Hookean model is used to derive the stretch ratio and update the tangent modulus of materials. The robot's compliance is obtained by integration with the forward kinematics building on the static Cosserat rod model. The derived compliance matrix is utilized to regulate robot's compliance along the $x$-, $y$-, and $z$-axes. Computational and experimental validation demonstrate high fidelity of the proposed approach. Moreover, experiments illustrate that the exhibited robot's compliance can be regulated up to 49.5% higher or 34.2% lower compared to inherent robot's compliance. The proposed model-based compliance control strategy has also demonstrated its effectiveness in enhancing grasping ability when implemented on a soft gripper.**

***Index Terms*—Compliance modeling and control, hyperelastic model, pneumatic-driven soft robots, statics and kinematics.**

## I. Introduction

PNEUMATIC-DRIVEN soft robots have been applied in various applications that require gentle interactions between the robot and its environment, due to their intrinsic compliance [1]. Such applications include soft grippers for delicate object grasping [2], [3] and soft medical tools designed for minimally invasive surgeries (MISs), such as transoral and endoluminal procedures [4], [5]. While stiffness-variable structures can regulate robot compliance, these mechanisms often compromise the robot's softness, require additional spaces and energy inputs, and exhibit slower response times [3], [6]. Achieving precise, on-demand compliance regulation, i.e., enabling higher or lower compliance along specific directions, is critical for enhancing robotic performance [4], [7], [8]. This capability allows robotic systems to increase stiffness for tasks requiring high-load capability, such as tissue clamping or cutting in MIS, while maintaining adequate compliance in other directions to ensure safe operation. However, achieving such on-demand compliance control remains fundamentally challenging when incorporating stiffening structures. Moreover, soft robots exhibit system nonlinearity and further complicate compliance control. These technical challenges demand new compliance modeling and control approaches.

Compliance nonlinearity of soft robots primarily results from two factors. First, soft materials feature hyperelasticity with a nonlinear stress–strain relationship [9], [10]. In this case, linear elastic material-based models, such as the Euler–Bernoulli [11] and the Timoshenko beam theory [12], inevitably result in modeling errors. As such, hyperelastic models are widely utilized in soft robots, such as the neo-Hookean model, Mooney–Rivlin model, and Ogden and [9], [13]. Second, the actuation principles, such as actuation pressure or embedded tendons [14], might introduce nonlinearity by varying mechanical properties of soft robots. For example, pressure-dependent factors were used to describe the varying stiffness properties of soft robots [15], [16], [17]. However, these works did not reveal how Cartesian

Received 9 September 2024; revised 8 January 2025; accepted 18 March 2025. Recommended by Technical Editor H. Su and Senior Editor C. Clevy. This work was supported in part by the Springboard Award of the Academy of Medical Sciences under Grant SBF003-1109, in part by the Engineering and Physical Sciences Research Council under Grant EP/R037795/1, Grant EP/S014039/1, and Grant EP/V01062X/1, in part by the Royal Academy of Engineering under Grant IAPP18-19\264, in part by the UCL Dean's Prize, in part by UCL Mechanical Engineering, and in part by the China Scholarship Council. *(Corresponding author: Helge A. Wurdemann.)*

Jialei Shi is with the Department of Mechanical Engineering, University College London, WC1E 7JE London, U.K., and also with the Mechatronics in Medicine, The Hamlyn Centre for Robotic Surgery, Department of Mechanical Engineering, Imperial College London, SW7 2AZ London, U.K. (e-mail: j.shi@imperial.ac.uk).

Sara-Adela Abad is with the Department of Mechanical Engineering, University College London, WC1E 7JE London, U.K., and also with the Universidad Nacional de Loja, Loja 110101, Ecuador (e-mail: s.abad-guaman@ucl.ac.uk).

Ge Shi is with the Department of Mechanical Engineering, University College London, WC1E 7JE London, U.K., and also with Robotics and Autonomous Systems Group, CSIRO, Pullenvale, QLD 4069, Australia.

Wenlong Gaozhang and Helge A. Wurdemann are with the Department of Mechanical Engineering, University College London, WC1E 7JE London, U.K. (e-mail: h.wurdemann@ucl.ac.uk).

Jian Sheng Dai is with the Institute of Robotics, Southern University of Science and Technology, Shenzhen 518055, China, and also with the Centre for Robotics Research, Department of Engineering, King's College London, WC2R 2LS London, U.K. (e-mail: jian.dai@kcl.ac.uk).

This article has supplementary material provided by the authors and color versions of one or more figures available at https://doi.org/10.1109/TMECH.2025.3553387.

Digital Object Identifier 10.1109/TMECH.2025.3553387

compliance of soft robots are impacted by these nonlinearities and varies under different robot configurations.

The investigation of compliance properties of soft robots has been explored. The robot compliance property depends on robot configurations and materials [18]. To analytically model how robot's compliance behaves with the robot configuration, [19] presented a compliance modeling method via the finite differentiation, where the elongation of the material was negligible. Similarly, finite differentiation of kinematics model was utilized to derive compliance matrices of parallel continuum robots and achieve compliance analysis [20]. [21] investigated how the tendons impact the compliance distribution of a continuum robot. Similar to rigid-linked robots, the Cartesian compliance of soft robots could be modeled using Jacobian mapping [22], and the dimension of Jacobian matrices depends on the numbers of discretized elements. Moreover, these compliance models were restricted to nonextensible robots and the material hyperelasticity was usually not modeled. To incorporate material nonlinearity into compliance modeling, [23] introduced an analytical approach using the screw theory and a parameterized piecewise constant curvature (PCC) model. Subsequently, a stiffness modeling and analysis framework for soft robots was developed using Lie theory [24]. Furthermore, recent study demonstrates that computational complexity can be eased via, e.g., interpolated polynomial [25], optimal control [26], Newtonian and Lagrangian models [27]; Nevertheless, these techniques remain to be investigated for compliance models.

Compliance regulation is essential for soft robots. Common techniques to regulate robot's compliance involve the incorporation of stiffening mechanisms [28], such as granular or layer jamming [2], [29], use of low melting point alloys (LMPA) [6], and a combination of tendon-driven and air pressurization [30]. In an effort to avoid the introduction of stiffening mechanisms, the antagonistic actuation approach has been developed [31]. For instance, a variable stiffness joint was presented in [32], employing two soft air chambers acting antagonistically on a single rotation joint. This actuator allows for various pressure combinations to achieve the same joint angle and permits adjustment of joint stiffness. The same antagonistic stiffening principle was also employed in [33] to vary the stiffness of soft robots constructed with pneumatic artificial muscles. However, the specialized structural design required by the antagonistic principle renders it less applicable for small-scaled soft continuum robots.

Research on model-based compliance and stiffness control for soft robots has also been conducted. The pioneering work in this area, without resorting to stiffening or antagonistic mechanisms, was outlined in [8]. In this approach, the controller actuates the robot to a deflected configuration to generate a prescribed tip force, achieving a desired tip stiffness. The robot kinematics was described using the Cosserat rod model. Similarly, the study detailed in [34] accomplished stiffness control for a parallel continuum robot based on estimated force and robot pose. The results demonstrated that the stiffness controller can vary the natural stiffness of soft robots by about a factor of two along the $x$- and $y$-axes. Building on a PCC assumption, a Cartesian stiffness control approach was proposed for a multisegment, tendon-driven soft robot [7]. This method defined desired compliance ellipsoids to formulate optimization objective functions

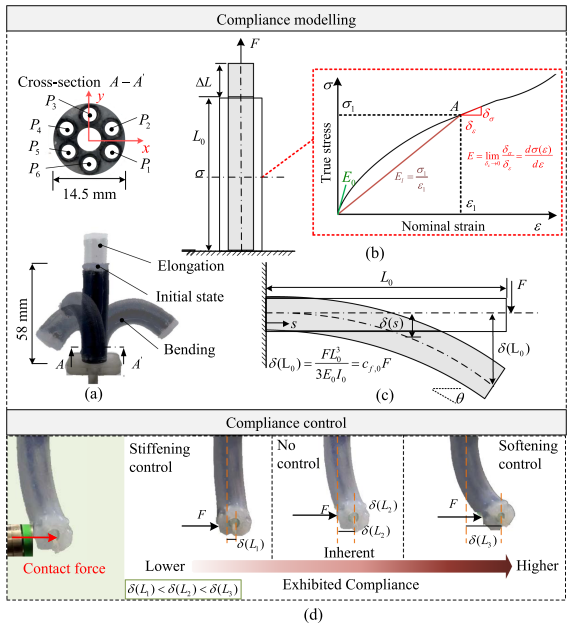


Fig. 1. Compliance modeling and control for soft robots. (a) Soft manipulator can achieve omnidirectional bending and elongation motions, with three chamber pairs actuated independently. (b) Illustration of the hyperelastic response. (c) Flexural compliance $c_{f,0} = \frac{L_0^3}{3E_0 I_0}$ when the robot has a deflection with a bending angle of $\theta$. (d) Illustration of the compliance control subjected to tip forces. The exhibited robot's compliance can be softer (softening control) or stiffer (stiffening control) than the inherent robot's compliance properties.

to obtain desired robot poses. The compliance of soft robots was regulated by adjusting the internal chamber pressure. Likewise, a tendon-tensioning method was proposed to control the stiffness of a dual-segment, tendon-driven soft robot based on depth vision. In this case, a closed-loop controller was designed for stiffness compensation [4]. Notably, in space-constrained applications, such asMIS, the size requirements of clinical settings could pose challenges to the implementation of feedback sensors or hybrid actuation principles [35].

In summary, though a significant amount of study has been done in kinematics and dynamics modeling techniques, especially for elastomer-based soft robots with nonlinear materials, model-based compliance analysis and control needs further research. This requires incorporating hyperelastic models into compliance modeling and to achieve active compliance control, particularly for pneumatic-driven soft robots without stiffening mechanisms or hybrid actuation principles.

This work proposes a compliance modeling and control approach for hyperelastic soft robots exhibiting material nonlinearity. The compliance control strategy is built on the established compliance model (see Fig. 1). The predicted longitudinal stretch ratio was first established via the neo-Hookean model, where the tangent modulus was derived from the nonlinear strain–stress curve. Based on that, the Cosserat rod theory was used to analytically derive the configuration-dependent compliance and achieve a model-based compliance control. Finally, simulations and experiments were compared to validate the model of robot's compliance and active compliance control under different robot's configurations.

| Initial state | Initial representation | Value | Update of parameters | |
|---|---|---|---|---|
| | | | Linear elasticity model | Proposed model |
| $R_{ro,0}$ | — | 7.25 mm | $R_{ro} = R_{ro,0}$ | $R_{ro} = R_{ro,0}/\sqrt{\lambda_1}$ |
| $R_{ri,0}$ | — | 2.25 mm | $R_{ri} = R_{ri,0}$ | $R_{ri} = R_{ri,0}/\sqrt{\lambda_1}$ |
| $R_{co,0}$ | — | 1.85 mm | $R_{co} = R_{co,0}$ | $R_{co} = R_{co,0}$ |
| $R_{ci,0}$ | — | 1.25 mm | $R_{ci} = \sqrt{(R_{co,0}^2(\lambda_1-1)+R_{ci,0}^2)/\lambda_1}$ | $R_{ci} = \sqrt{(R_{co,0}^2(\lambda_1-1)+R_{ci,0}^2)/\lambda_1}$ |
| $R_{cp,0}$ | — | 4.75 mm | $R_{cp} = R_{cp,0}$ | $R_{cp} = R_{cp,0}/\sqrt{\lambda_1}$ |
| $A_0$ | $A_0 = \pi(R_{ro,0}^2 - R_{ri,0}^2 - 6R_{ci,0}^2)$ | 119.77 mm$^2$ | $A = A_0$ | $A = A_0/\lambda_1$ |
| $d_{i,0}$ | $d_{i,0} = \begin{bmatrix}\cos\phi_i & -\sin\phi_i & 0\\ \sin\phi_i & \cos\phi_i & 0\\ 0 & 0 & 1\end{bmatrix}\begin{bmatrix}R_{cp,0}\\ 0\\ 0\end{bmatrix}$ | — | $d_i = \begin{bmatrix}\cos\phi_i & -\sin\phi_i & 0\\ \sin\phi_i & \cos\phi_i & 0\\ 0 & 0 & 1\end{bmatrix}\begin{bmatrix}R_{cp,0}\\ 0\\ 0\end{bmatrix}$ | $d_i = \begin{bmatrix}\cos\phi_i & -\sin\phi_i & 0\\ \sin\phi_i & \cos\phi_i & 0\\ 0 & 0 & 1\end{bmatrix}\begin{bmatrix}R_{cp}\\ 0\\ 0\end{bmatrix}$ |
| $I_{x,0}$ | $I_{x,0} = \pi(R_{ro,0}^4 - R_{ri,0}^4)/4 - \sum_i^6(\pi R_{ci,0}^4/4 + \lvert d_{i,0}\rvert_x^2 \pi R_{ci,0}^2)$ | 1806.02 mm$^4$ | $I_x = \pi(R_{ro,0}^4 - R_{ri,0}^4)/4 - \sum_i^6(\pi R_{ci,0}^4/4 + \lvert d_{i,0}\rvert_x^2 \pi R_{ci,0}^2)$ | $I_x = \pi(R_{ro}^4 - R_{ri}^4)/4 - \sum_i^6(\pi R_{ci}^4/4 + \lvert d_i\rvert_x^2 \pi R_{ci}^2)$ |
| $J_{z,0}$ | $J_{z,0} = \pi(R_{ro,0}^4 - R_{ri,0}^4)/2 - \sum_i^6(\pi R_{ci,0}^4/4 + \lvert d_{i,0}\rvert^2 \pi R_{ci,0}^2)$ | 3623.54 mm$^4$ | $J_z = \pi(R_{ro,0}^4 - R_{ri,0}^4)/2 - \sum_i^6(\pi R_{ci,0}^4/4 + \lvert d_{i,0}\rvert^2 \pi R_{ci,0}^2)$ | $J_z = \pi(R_{ro}^4 - R_{ri}^4)/2 - \sum_i^6(\pi R_{ci}^4/4 + \lvert d_i\rvert^2 \pi R_{ci}^2)$ |
| $E_0$ | $E_0 = 3\mu_0$ | 130 kPa | $E_l = 83$ kPa | $E_l = \frac{E_0}{3}\left(\frac{2\varepsilon_{l,e}^3 + 6\varepsilon_{l,e}^2 + \varepsilon_{l,e} + 3}{(1+\varepsilon_{l,e})^2}\right)$ |

(a)

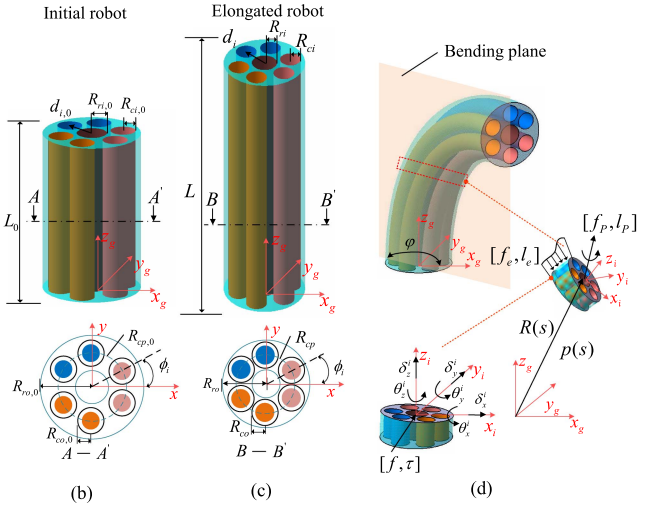


(b) (c) (d)

Fig. 2. Parameters and notations. (a) This table lists system parameters and their updates in the linear model-based and the proposed neo-Hookean-based approach. $E_l$ is defined in Fig. 1. (b) Initial state of the robot with the dimensions. (c) Actuated robot with updated dimensions. (d) Illustration of an extracted element of the bent robot with the coordinates used in Section II-C2. As shown in (b) and (c), two adjacent chambers (in the same color) are connected.

Our contributions are summarized as follows.

1) A novel neo-Hookean model-based static compliance modeling approach is proposed and validated for pneumatic-driven, hyperelastic soft robots. The influence of the material hyperelasticity on the Cartesian compliance is considered.
2) A compliance control approach is presented based on the modeled compliance matrices. This approach enables the regulation of the robot's Cartesian compliance, allowing for achieving both higher (softening control) or lower (stiffening control) compliance compared to the inherent robot's compliance properties. To the best of our knowledge, this work for the first time realizes the compliance regulation for the pneumatic-driven soft continuum robot without employing stiffening mechanisms or hybrid actuation principles.

The rest of this article is organized as follows. Section II details the compliance model, followed by the numerical implementation and the dimensionless compliance analysis. The model-based compliance control strategy is then presented. The validation is given in Section III, where compliance modeling and control approach is thoroughly investigated by both simulations and experiments. Section IV discusses the proposed compliance modeling and control method based on the validation results. Finally, Section V concludes this article.

## II. Methodology of Static Compliance Modeling and Control

### A. Soft Robot Prototype

The soft robot is pneumatically driven and made of silicone [Ecoflex 00–50 Supersoft, SmoothOn]. Such soft robots are inherently compliant and safe when interacting with environments. As such, they can be used in various applications, e.g., soft instruments for MIS [36] and soft grippers. The robot has three reinforced actuation chamber pairs to constrain the radial inflation while allowing elongation. By actuating different chamber pairs, the robot can achieve omnidirectional bending and elongation motions [see Fig. 1(a)]. Moreover, the free central lumen is designed for feeding through instruments (e.g., sensors or cameras) attached at the robot's tip. Dimension details are in Fig. 2. The robot fabrication is in [10]. Since the robotic prototype features reinforced circular actuation chambers, the pressurization does not alter the shape and parameter of these chambers, due to the nonstretchable reinforcement layer [13]. As such, it can assume that the robot's cross-section remains circular and experiences uniaxial deformation when the robot elongates.

### B. Neo-Hookean Model

Hyperelastic models are built upon the strain density function $\Pi$ using strain invariants. The first invariant $I_1$ is defined as a function of the axial stretch ratio $\lambda_1$, the circumferential stretch ratio $\lambda_2$, and the radial stretch ratio $\lambda_3$, yielding $I_1 = \lambda_1^2 + \lambda_2^2 + \lambda_3^2$. The second invariant $I_2 = \lambda_1^2\lambda_2^2 + \lambda_2^2\lambda_3^2 + \lambda_1^2\lambda_3^2$. Silicone materials are incompressible $(\lambda_1\lambda_2\lambda_3 = 1)$, and the robot undergoes uniaxial loading $\lambda_2 = \lambda_3 = \frac{1}{\sqrt{\lambda_1}}$. The principal Cauchy stress constitutive model [9] yields

$$\sigma_{1,t} = 2\left(\lambda_1^2 - \frac{1}{\lambda_1}\right)\left(\frac{\partial \Pi}{\partial I_1} + \frac{1}{\lambda_1}\frac{\partial \Pi}{\partial I_2}\right) \tag{1}$$

where $\sigma_{1,t}$ is the true axial stress, $I_1 = \lambda_1^2 + \frac{2}{\lambda_1}$, and $I_2 = 2\lambda_1 + \frac{1}{\lambda_1^2}$. The relationship between the axial engineering strain $\epsilon_{1,e}$ and $\lambda_1$ is $\lambda_1 = 1 + \epsilon_{1,e}$.

The neo-Hookean model is especially suitable when the stretch ratio is less than 1.5 [13], with $\Pi = \frac{\mu_0}{2}(I_1 - 3)$. Based on (1), the true stress $\sigma_{1,t}$ is obtained as

$$\sigma_{1,t} = \mu_0\left(\lambda_1^2 - \frac{1}{\lambda_1}\right) = \frac{E_0}{3}\left(\frac{\epsilon_{1,e}^3 + 3\epsilon_{1,e}^2 + 3\epsilon_{1,e}}{1 + \epsilon_{1,e}}\right) \tag{2}$$

where $\mu_0$ is the effective initial shear modulus, and $E_0$ is the effective initial Young's modulus. Engineering stress is denoted by $\sigma_{1,e}$, then $\sigma_{1,t} = \lambda_1\sigma_{1,e}$.

The rubber volume $V_{cv}$ of one reinforced chamber is $V_{cv} = \pi(R_{co,0}^2 - R_{ci,0}^2)L_0$, where $R_{co,0}$ is the initial outer chamber radius, $R_{ci,0}$ is the initial inner chamber radius, and $L_0$ is the initial length of the chamber. Due to the chambers are densely reinforced by in-extensible thread, there is no circumferential strain of chambers after pressurization [13], which means $R_{co} = R_{co,0}$. The inner chamber diameter $R_{ci}$ with an axial stretch of $\lambda_1$ can be approximated by

$$R_{ci} = \sqrt{R_{co,0}^2(\lambda_1 - 1) + R_{ci,0}^2}/\sqrt{\lambda_1}. \tag{3}$$

The force generated by the pressure $F_P$ then can be calculated as $F_P = \sum_{i=1}^{6} P_i A_c = \sum_{i=1}^{6} P_i \pi R_{ci}^2$, $P_i$ is pressure in the $i$th chamber, $A_c$ is the chamber area. Similarly, the cross-section area $A$ of the robot is described by

$$A = A_0/\lambda_1 = \pi\left(R_{ro,0}^2 - R_{ri,0}^2 - 6R_{ci,0}^2\right)/\lambda_1. \tag{4}$$

$R_{ro,0}$ is the initial outer radius of the robot, $R_{ri,0}$ is the initial radius of the inner lumen. The force in the axial direction is balanced by pressure and the internal stress, yielding

$$F_\lambda = A\sigma_{1,t} = F_P \tag{5}$$

where $F_\lambda$ is the internal force. Substituting (2)–(4) into (5), the axial stretch $\lambda_1$ can then be solved numerically based on the $E_0$, $R_{co,0}$, $R_{ci,0}$, $R_{ri,0}$, $R_{ro,0}$, and $P_i$. Note that (5) is a third-order equation, and the two complex solutions are ignored. $\lambda_1$ can be used to achieve the kinematics modeling [13], [15].

### C. Neo-Hookean Model-Based Compliance Model

In this section, we present a neo-Hookean model-based compliance modeling approach, inspired by the work from [24]. Here, the nonlinear strain–stress is described using a hyperelastic model, and the robot kinematics is established using the Cosserat rod model. The Cosserat rod model is valid in a small strain regime when employing linear constitutive models [37]. To accommodate the nonlinear hyperelasticity, this work updates the cross-section dimensions of the elongated soft robot [see Fig. 2(a)] and the tangent modulus utilizing the stretch ratio $\lambda_1$ from solving (5). The following model builds on the elongated soft robot [see Fig. 2(c)].

*1) Static Kinematics Model:* The pressurized chambers introduce a distributed force $f_P(s)$ and moment $l_P(s)$ along the robots [24], [37]. Since the stretch $\lambda_1$ has been solved for the elongated robot, the actuation pressure only produces the distributed moment $l_P(s)$, and $f_P(s) = 0$. Here, the differentiation with respect to the central curve length $s$ ($s \in [0, L]$) of soft robots, is denoted by $(\cdot)_s$. The equilibria of the force and moment of the elongated soft robot along the arc $s$ are

$$n_s(s) = -f_e(s), \quad m_s(s) = -\hat{p}_s(s)n(s) - l_e(s) + l_P(s). \tag{6}$$

The position vector $p(s)$ and the orientation matrix $R(s)$ along the arc $s$ is described by

$$p_s(s) = R(s)v(s), \quad R_s(s) = R(s)\hat{u}(s) \tag{7}$$

where $n(s)$ and $m(s)$ are the internal force and moment along the arc $s$. $f_e(s)$ and $l_e(s)$ are the distributed external force and moment. $v(s)$ and $u(s)$ are the strain and the curvature vectors expressed in the body frame, respectively. $\hat{(\cdot)}$ is the mapping from $\mathbb{R}^3$ to $\mathfrak{so}(3)$ [37]. $l_P(s)$ in (6) is calculated as

$$l_P(s) = \sum_{i=1}^{6} P_i A_c R(s)[(v(s) + \hat{u}(s)d_i) \times e_3 + \hat{d}_i\hat{u}(s)e_3)] \tag{8}$$

where $d_i$ is the position vector pointing from the center of the robot to the center of the chamber with $d_i = \frac{d_{i,0}}{\sqrt{\lambda_1}}$ [see Fig. 2(c)]. $d_{i,0}$ is the initial value and $e_3 = [0, 0, 1]^T$ is a unit vector. Using linear constitutive equations, $n(s)$ and $m(s)$ are

$$n(s) = R(s)k_{se}(v(s) - e_3), \; m(s) = R(s)k_{bt}u(s). \tag{9}$$

$k_{se} = \text{diag}[GA, GA, EA]$ is the stiffness density matrix for shear and elongation. $G$ is the shear modulus. $k_{bt} = \text{diag}[EI_x, EI_y, GJ_z]$ is the stiffness density matrix for bending and twisting. $I_x$, $I_y$, and $J_z$ are the second moment of area around the $x$-, $y$-, and $z$-axes, related to $\lambda_1$. $k_{se}$ and $k_{bt}$ are constant along the arc $s$. Fig. 2 reports their calculations. $|d_i|$ is the length of $d_i$. $|d_i|_x$ is the projection of $d_i$ onto the $x$-axis.

From (2), it can be observed that the material modulus varies with strains. The tangent modulus $E_t$ can be described as

$$E_t = \frac{\mathrm{d}\sigma_{1,t}}{\mathrm{d}\epsilon_{1,e}} = \frac{E_0}{3}\left(\frac{2\epsilon_{1,e}^3 + 6\epsilon_{1,e}^2 + 6\epsilon_{1,e} + 3}{(1 + \epsilon_{1,e})^2}\right) \tag{10}$$

where $\sigma_{1,t}$ comes from the function in (2). $E_t$ is determined by the initial Young's modulus $E_0$ and strain $\epsilon_{1,e}$. $G$ can then be calculated as $G = \frac{E}{3}$. $k_{se}$ and $k_{bt}$ can now be determined based on the neo-Hookean model. Notably, by establishing the Cosserat model on the elongated robot, we address material nonlinearity through linear constitutive models [see (9)]. This is achieved by solving $\lambda_1$ from the neo-Hookean model and updating the stiffness density matrices $k_{se}$ and $k_{bt}$ accordingly [see Fig. 2(a)].

*2) Compliance Modeling:* A compliance matrix $C$ is

$$\mathbf{T} = C\mathbf{W} \tag{11}$$

where the wrench $\mathbf{W} = [f_x, f_y, f_z, \tau_x, \tau_y, \tau_z]^T$ includes a force vector $f = [f_x, f_y, f_z]^T$ and a moment vector $\tau = [\tau_x, \tau_y, \tau_z]^T$. The twist $\mathbf{T} = [\delta_x, \delta_y, \delta_z, \theta_x, \theta_y, \theta_z]^T$ includes a displacement vector $\delta = [\delta_x, \delta_y, \delta_z]^T$ and an angle vector $\theta = [\theta_x, \theta_y, \theta_z]^T$.

The compliance density matrix $c^b$ written in the body frame can be calculated using $k_{se}$ and $k_{bt}$ by $c^b = \text{diag}[k_{se}^{-1}, k_{bt}^{-1}] = \text{diag}[GA, GA, EA, EI_x, EI_y, GJ_z]^{-1}$. The compliance of the soft robot is the aggregated compliance of serially connected elements. To achieve this, the element compliance in the body frame $\{x_i, y_i, z_i\}$ needs to be shifted to a same global frame $\{x_g, y_g, z_g\}$ via the adjoint matrix $\text{Ad}_{gi}(s)$. $\text{Ad}_{gi}(s)$ is constructed by the rotation matrix $R_{gi}(s)$ and the position vector $p_{gi}(s)$ [24]. Integrating the compliance along the robot gives the compliance of the robot at any position [24], yielding

$$C_i^g(s) = \int_0^{L_i} \text{Ad}_{gi}^{-T}(s)c^b\text{Ad}_{gi}^{-1}(s)\mathrm{d}s \tag{12}$$

where $C_i^g(s)$ is the total compliance in the global frame at the position of $s = L_i$, and $L_i$ is the integration curve length. Combining (6), (7), (9), and (12), the kinematics and robot compliance for an elongated robot can be described by

$$\begin{cases} p_s(s) = R(s)v(s), \;\; v(s) = k_{se}^{-1} R^T(s) n(s) + e_3 \\ R_s(s) = R(s)\hat{u}(s), \;\; u(s) = k_{bt}^{-1} R^T(s) m(s) \\ n_s(s) = -f_e(s) \\ m_s(s) = -\hat{p}_s(s) n(s) - l_e(s) + l_P(s) \\ (C_i^g(s))_s = \mathrm{Ad}_{gi}^{-T}(s) c^b \mathrm{Ad}_{gi}^{-1}(s) \end{cases} \tag{13}$$

with the integration interval as $[0, L]$ and $E = E_t = \frac{\mathrm{d}\sigma_{1,t}}{\mathrm{d}\epsilon_{1,e}}$. This establishes the configuration-dependent compliance model based on the neo-Hookean model. It is worth noting that (13) describes the neo-Hookean model-based compliance modeling and further extends the framework proposed in [24]. Here, the neo-Hookean model describes a nonlinear strain–stress relation and derives the stretch $\lambda_1$ in a single step by solving (5). In contrast, the nonlinear material property is considered using an iterative compensation approach in multiple steps [24].

Here, the derived compliance matrix has a dimension of $6 \times 6$ and is symmetrical [24], with a block-form of

$$C = \begin{bmatrix} C_{11} & C_{12} \\ C_{21} & C_{22} \end{bmatrix} \tag{14}$$

where the blocks $C_{21} = C_{12}^T$. This property can be utilized to lighten the computation of (12) by only calculating $C_{11}, C_{21}$ and $C_{22}$. Each block has of a dimension of $3 \times 3$.

### D. Numerical Implementation and Compliance Analysis

*1) Numerical Implementation:* The distributed external force $f_e(s)$ only contains the gravity vector $g$, and no distributed moment is present, so $f_e(s) = \rho g A$, $l_e(s) = 0$, and $\rho$ is the material density. Finally, (13) can be integrated by the fourth-order Runge–Kutta scheme [38]. To achieve the numerical integration, the state variables $y$ should be in a vector form, so we choose $y$ as $[p, R_{vc}, m, n, C_{vc}]_{45\times1}^T$ in (13), where $C_{vc}$ is a $1 \times 27$ vector and contains all the entities of $C_{11}, C_{12}$, and $C_{22}$ from the $6 \times 6$ compliance matrix $C$, with $C_{vc}(0)$ as a $1 \times 27$ zero vector. The initial state of $p(0)$ is $[0, 0, 0]$, and $R_{vc}(0)$ equals reshaping a $3 \times 3$ identity matrix to a $1 \times 9$ vector. Initial conditions $[n(0), m(0)]$ are unknown, (13) is solved using the shooting method [37]. When there is no external tip moment, the boundary conditions are

$$n(L) = n_e(L), \;\; m(L) = R(L) \sum_{i=1}^{6} (d_i \times A_c P_i e_3) \tag{15}$$

where $n(L)$ and $m(L)$ are the integrated force and moment at the tip position, $n_e(L)$ is the external tip force. For the elongated soft robot, forces from the actuated chambers should be excluded when formulating the boundary condition of $n(L)$.

*2) Dimensionless Compliance Analysis:* A compliance matrix has the form of (14). To illustrate the results and analyze the robot's compliance in a general way, a dimensionless compliance analysis [21] is adopted. The dimensionless flexural compliance $\gamma_c$ and the dimensionless load location $\xi$ with respect to the length of the robot can be defined as

$$\gamma_c = \frac{3E_0 I_0}{L_0^3} \frac{\delta(\xi)}{F(\xi)}, \quad \xi = \frac{s}{L} \tag{16}$$

where $\delta(\xi)$ is the resultant displacement when $F(\xi)$ is applied at position $\xi$. $\delta(\xi)$ can be obtained via multiplying compliance matrix (13) by a small $F(\xi)$. $\gamma_c$ reveals how the compliance evolves with respect to the initial flexural compliance $c_{f,0}$ at the tip position of the un-actuated soft robot (see Fig. 1).

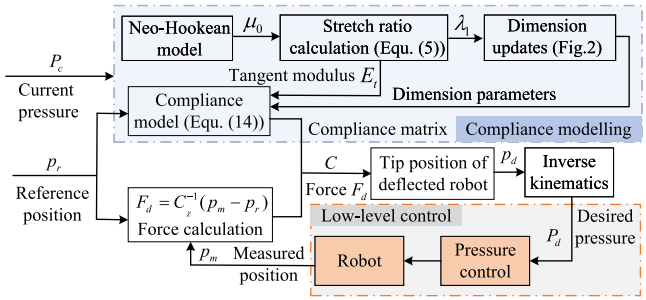


Fig. 3. Diagram of the compliance controller, building on the compliance model from Section II-C using the neo-Hookean model (see Section II-B). The IK solver is elaborated in [17].

### E. Model-Based Tip Compliance Control Strategy

To demonstrate the effectiveness of the established compliance model, this section further presents a compliance control strategy to regulate robot's compliance in specific directions [8] when interacting with environments. The directional compliance control is critical for certain tasks, e.g., inserting a peg into a hole [7] or manipulating tissue [8]. The block diagram of the compliance controller is in Fig. 3.

When the measurement tip position $p_m$ is away from the reference tip position $p_r$, $p_m - p_r = C_{\chi,m} \Delta F$. $\Delta F$ is the applied tip force. The compliance control needs to regulate the compliance matrix $C_{\chi,m}$. This work aims to regulate compliance responses along the $x$-, $y$-, and $z$-axes independently. To this end, a control gain matrix $C_\chi$ is defined as

$$C_\chi = \begin{bmatrix} \chi_x^{-1} & 0 & 0 \\ 0 & \chi_y^{-1} & 0 \\ 0 & 0 & \chi_z^{-1} \end{bmatrix} \tag{17}$$

where $\chi_x, \chi_y$, and $\chi_z$ are gain factors along three axes. A virtual desired tip force vector $F_d$ is defined as

$$F_d = C_\chi^{-1} (p_m - p_r). \tag{18}$$

By substituting $F_d$ from (18) and the tip compliance $C$ from (13) into (11), the desired tip position $p_d$ is obtained. The desired control pressure $P_d$ is determined by solving the inverse kinematics (IK). In the field of soft robotics, inverse control involves determining the necessary actuator inputs to achieve desired positions and/or orientations in the Cartesian space [22]. In this study, the actuator input is the actuation pressure. Details of the adopted IK solver are in [17], where the robot kinematics is built on the static Cosserat model.

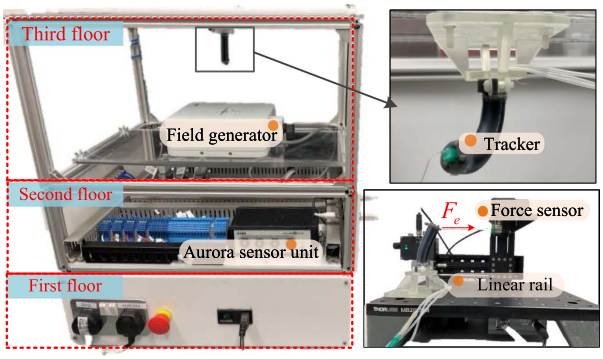


Fig. 4. Overview of the experimental setup, with details reported in [39].

## III. Computational and Experimental Validation

### A. Experimental Setup

Fig. 4 reports the experimental setup. The chamber pressure is regulated and monitored by regulators [Camozzi K8P]. The pressure regulators can be controlled by a data acquisition device [NI-DAQ USB-6341] or a microcontroller [Arduino DUE]. The force is measured by an F / T sensor [IIT-FT17]. A linear rail [Zaber X-LSM100A] can pull the robot using the given displacements to measure robot compliance. An electromagnetic system [NDI Aurora] monitors the robot's tip position. The position measurement exhibits a root-mean-square error (RMSE) of 0.7 mm.

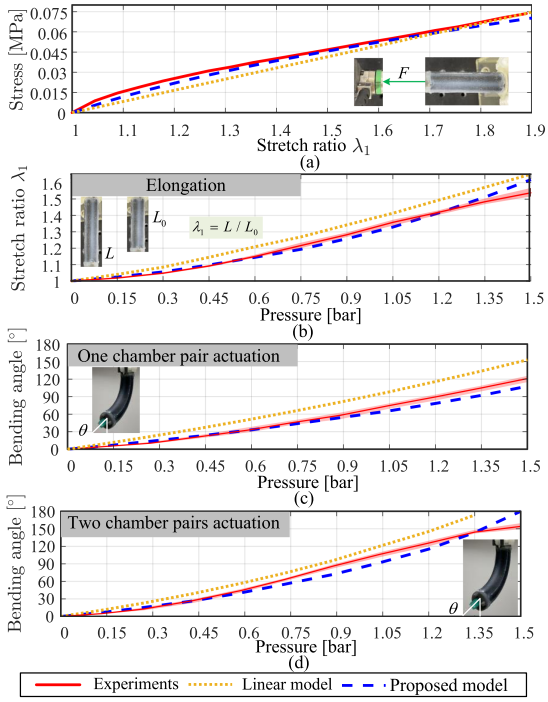


Fig. 5. Results for Experiment 1—Nonlinear responses. (a) Comparison of the stretch–strain curve of the proposed neo-Hookean-based model and linear model. (b) Results of the pressure–stretch curve. The results of the pressure–bending angle curves, with (c) one chamber pair actuated, (d) two chamber pairs actuated. The shaded red lines in (b)–(d) are the experimental stretch ratios and bending angles of three trials.

### B. Experimental Protocols

*1) Experiment 1 - Hyperelasticity Response:* The value of $\mu_0$ was identified by the measured stress–strain curve with a maximum stretch ratio of 1.9. Three sets of experiments were then run to validate the hyperelasticity response. In the elongation test, all chambers were pressurized; in the one chamber pair bending test, the pressure sequence is $P_{1,2} \rightarrow P_{3,4} \rightarrow P_{5,6}$; in the two chamber pairs bending test, the pressure sequence is $P_{1,2,3,4} \rightarrow P_{3,4,5,6} \rightarrow P_{5,6,7,8}$ [see Fig. 1(a)]. The elongation and bending angle were recorded by the tracker. The pressure increment was 0.15 bar and the maximum pressure was set as 1.5 bar. Each test has three trials.

*2) Experiment 2 - Kinematics Validation:* Six trials [experiment (2a)–(2f)] were run, including three one chamber pair actuation sets and three two chamber pairs actuation sets. The pressure was chosen in the form of triangle wave to simulate the quasistatic case. In the one chamber pair actuation test, the pressurization sequences were $P_{5,6} \rightarrow P_{3,4} \rightarrow P_{1,2}$ (2a), $P_{1,2} \rightarrow P_{3,4} \rightarrow P_{5,6}$ (2b), and $P_{5,6} \rightarrow P_{1,2} \rightarrow P_{3,4}$ (2c), respectively. The maximum amplitude values of each pressure wave were 0.9, 1.2, and 1.5 bar. In the two chamber pairs actuation test, the pressurization sequences were $P_{1,2,5,6} \rightarrow P_{3,4,5,6} \rightarrow P_{1,2,3,4}$ (2 d), $P_{1,2,5,6} \rightarrow P_{1,2,3,4} \rightarrow P_{3,4,5,6}$ (2e), and $P_{3,4,5,6} \rightarrow P_{1,2,5,6} \rightarrow P_{1,2,3,4}$ (2f), respectively [see Fig. 1(a)]. The maximum amplitude values of each wave were 0.6, 0.9 and 1.2 bar. In all tests, the maximum bending angle was about 120°.

*3) Experiment 3 - Dimensionless Compliance Validation and Analysis:* $\varphi$ defines the angle between the bending plane and the $x$–$z$ plane [see Fig. 2(d)]. When the bending plane is out of the $x$–$z$ plane, $\varphi$ is not 0° or 180°. The compliance along the $x$-, $y$-, and $z$-axes were all validated when the robot bends within and out of the $x$–$z$ plane. A movable plate was attached to three different positions along the robot, i.e., $0.5L$, $0.75L$, and $L$, to identify the compliance with different values of $\xi$ [see (16)]. The plate was pulled by the force sensor via a thin nickel wire, where the pulling displacement $\delta_e$ was controlled by the linear rail and the pulling force was given as $F_e$ (shown in Fig. 4). $P_{1,2}$ and $P_{3,4}$ were actuated to generate bending motions with $\varphi = 180°$ and $\varphi = -60°$, respectively. The maximum pressure in both cases was 1.5 bar with an increment of 0.3 bar. In each configuration, the compliance along the $x$-, $y$-, and $z$-axes was identified over three trials.

*4) Experiment 4 - Tip Compliance Control:* The soft robot was actuated to two configurations, with the desired tip positions of [20, 0, 44] mm and [10, –10, 44] mm for Configuration 1 (Conf. 1) and Configuration 2 (Conf. 2). Consequently, the corresponding angles $\varphi$ for Conf. 1 and Conf. 2 are 0° and –45°, respectively. Tip loads were applied using external calibrated weights [see Fig. 8(a)], and a tracker was attached at the robot tip to record the deflection distances under varying tip loads. To identify compliance responses along the $x$- and $y$-axes, tip loads of 0, 2.5, 5 g, and 7.5 g were used. In addition, compliance along the $z$-axis was measured under tip loads of 0, 5, 10, and 15 g. The gain factors [see (17)] were set as [–1, 0, 2, 4] and [–5, 0, 5, 10] when identifying robot's compliance along the $x$-/$y$-axis and $z$-axis, respectively.

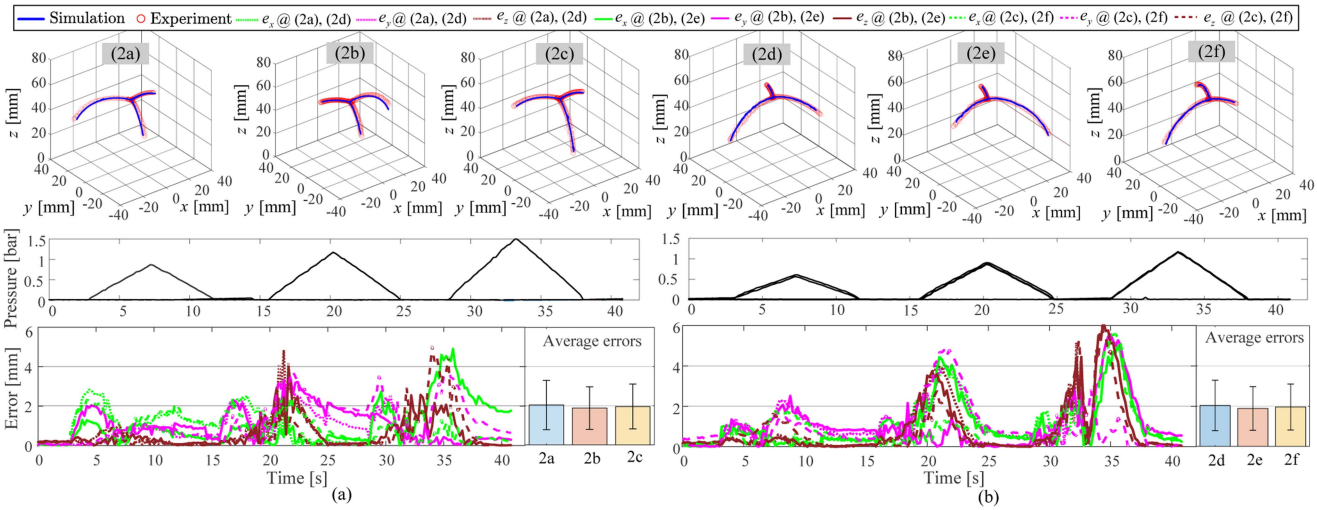


Fig. 6. Results for Experiment 2—Kinematics validation in two scenarios. (a) One chamber pair actuation and (b) two chamber pairs actuation. Simulated and experimental tip positions of the robot from (2a)–(2f) in the Cartesian space are shown at the top; the illustration of the pressure sequence is in the middle; the summarized absolute position errors $|e_x|$ in the $x$-axis, $|e_y|$ in the $y$-axis, and $|e_z|$ in the $z$-axis are shown at the bottom. The barplot summarizes the average values and standard deviations of $\sqrt{|e_x|^2+|e_y|^2+|e_z|^2}$.

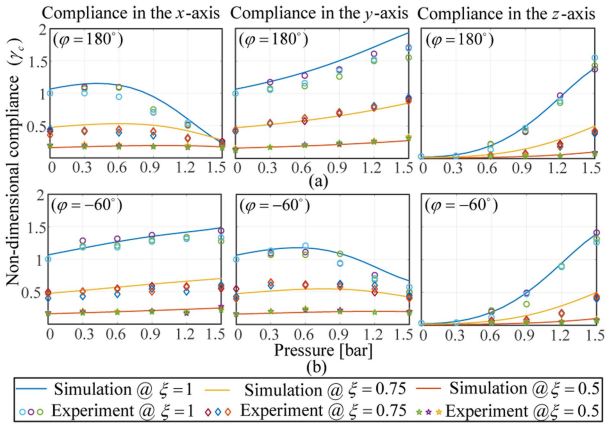


Fig. 7. Results for Experiment 3 - Validation of the dimensionless compliance $\gamma_c$ [defined by (16)]. The experimental and simulated compliance along three axes when $\varphi = 180°$ and $\varphi = -60°$ are shown in (a) and (b), respectively.

To quantify the compliance variation under different gain factors, the compliance variation ratio $\beta$ is defined as

$$\beta = \frac{C_{\chi,m} - C_{\chi|0,m}}{C_{\chi|0,m}} \times 100\% \tag{19}$$

which describes the variation of measured tip $C_{\chi,m}$ compliance (when $C_\chi$ is nonzero) compared to the robot's inherent compliance $C_{\chi|0,m}$ when $C_\chi$ is set as zero.

*5) Experiment 5 - Real-World Application on a Soft Gripper:* A real-world application involves using the compliance controller to improve the grasping capabilities of soft grippers. To explore this, a soft gripper was designed with three identical manipulators [see Fig. 10(a)]. The gripper was tested by grasping strawberries, raspberries, and cherries. During tests, the gripper was first commanded to grasp different objects using the same pressure. A probe then released the grasped objects by pushing them downward until they fell. Each object is being dropped three times, with and without compliance control implemented. Gain factors $\chi_x$, $\chi_y$, and $\chi_z$ were set to 4, 2, and 10, respectively. Forces between the probe and the objects were measured using the F/T sensor. The contact forces were calculated as the magnitude of force vectors.

## C. Results

*Results for Experiment 1:* Fig. 5(a) reports the stretch–stress curve, where the neo-Hookean model has the fitted value of $E_0$ as $1.3 \times 10^5$ Pa using the least square regression, and $E_l$ is linearized as $\frac{0.745\times10^6}{0.9} = 0.83 \times 10^5$ Pa, when the strain is 100%. Fig. 5(a) reveals that the linearized $E_l$ is smaller than the experimental value, especially when the stretch ratio is smaller than 1.5, In contrast, the neo-Hookean model can capture the nonlinear responses. Fig. 5(b) illustrates a nonlinear elongation and demonstrates that the linearized model consistently yields higher stretch ratios, with the RMSE as 0.06. By comparison, the proposed model exhibits a higher accuracy, with the RMSE value as 0.03. In addition, the proposed model exhibits a higher elongation than experiment when the pressure exceeds 1.2 bar, e.g., the simulated elongation ratio is 0.05 higher than the measured value. Fig. 5(c) and (d) show that the linear model has larger bending angles than experiments, with the RMSE values of 20.80° and 14.23° in one chamber pair actuation and two chamber pairs actuation tests. The proposed model outperforms, with RMSE values of 7.99° and 11.32°.

*Results for Experiment 2:* Fig. 6(a) reports the results of (2a)–(2c) with one chamber pair actuated, where the maximum position errors in all directions are within 5.10 mm. The errors increase with the pressure, e.g., when the pressure reaches 1.5 bar, the maximum $|e_x|$, $|e_y|$, and $|e_z|$ are 4.90, 4.67, and 5.05 mm, respectively. In contrast, those errors are 2.83, 2.03, and 1.05 mm when the maximum pressure is 0.9 bar. Fig. 6(b)

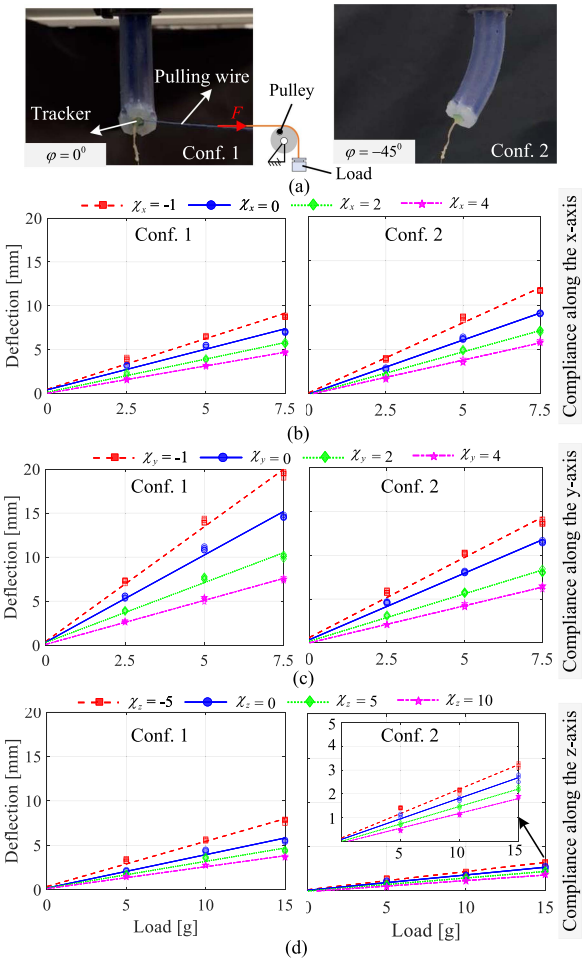


Fig. 8. Results for Experiment 4—Tip compliance control along three axes when the soft robot is actuated to two configurations. (a) Illustration of the experimental setup for compliance identification and two robot configurations. Tip compliance responses along the (b) $x$-, (c) $y$-, and (d) $z$-axes when tip loads vary. The robot's compliance, i.e., the line gradient, is fitted using a linear regression, and the identified compliance values are summarized in Table I.

shows a similar modeling performance. The maximum error in this scenario increases to 6.42 mm. In most cases, the maximum position errors are within 5 mm, i.e, less than 8.3% of the robot original length. In all tests, the average Cartesian tip position errors are between 1.88 and 2.03 mm, i.e., 3.1%∼3.4% of the robot's length.

*Results for Experiment 3:* Fig. 7(a) presents the results of the dimensionless compliance $\gamma_c$ when $\varphi = 180°$. $\gamma_c$ along the $x$-axis varies with the pressure, which first increases to 1.15 before decreasing to 0.23 when the pressure is 1.5 bar, about four times smaller than the initial value. On the contrary, the compliance along the $y$- and $z$-axes monotonically increases at high pressures; however, the variation in the $y$-axis is much smaller than that in the $z$-axis. For instance, the tip compliance $\gamma_c$ along the $y$-axis increases from 1 to 1.79, whilst that value along the $z$-axis varies from 0.02 to 1.39. Fig. 7(b) illustrates the compliance response when $\varphi = -60°$. Comparing to Fig. 7(a), (b) indicates a nonmonotonic compliance response in the $y$-axis, e.g., the tip compliance increases to 1.18 then reduces to 0.67.

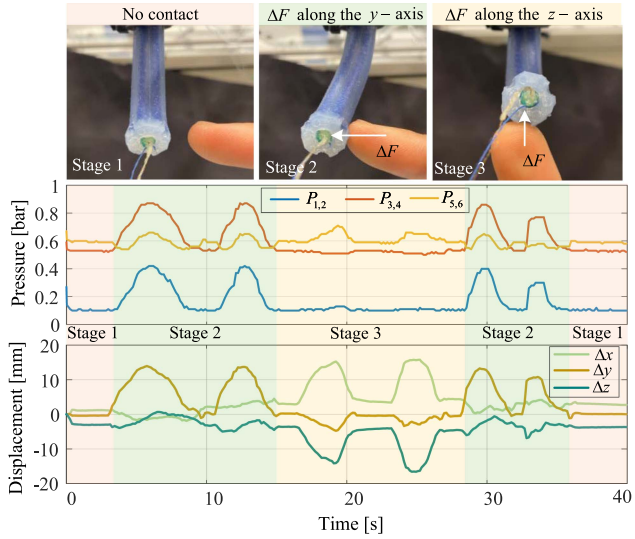


Fig. 9. Results for Experiment 4—Illustration of the monitored pressure and tip displacements when $\chi_y = 3$. The robot is in Conf. 1. The external force $\Delta F$ is along the $y$-axis in stage 2 and along the $z$-axis in stage 3. $\Delta x$, $\Delta y$ and $\Delta z$ are the components of $p_m - p_r$ [see (18)] in the $x$-, $y$-, and $z$-axes.

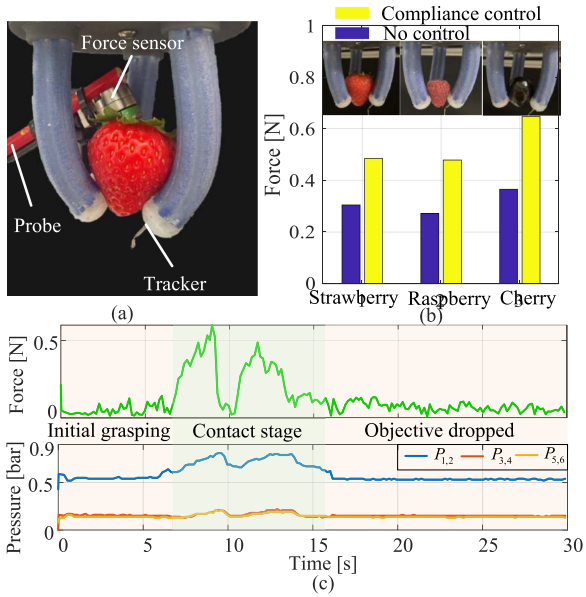


Fig. 10. Results for Experiment 5—(a) Soft gripper in experiments. (b) Force results when grasping different objectives with and without compliance control. (c) Interaction force and pressure in one trial with compliance control.

The compliance responses along the $z$-axis from Fig. 7(a) and (b) are similar. Fig. 7 also reports the model accuracy. The predicted compliance along the $z$-axis in both cases are the most accurate, with the dimensionless error less than 0.1. The largest errors come from the tip compliance in the $x$-axis when $\varphi = 180°$ and in the $y$-axis when $\varphi = -60°$, where the maximum dimensionless errors can reach $0.15 \sim 0.25$. In most cases, the discrepancy of $\gamma_c$ is below 0.1. Furthermore, the compliance shares a similar response with the pressure when $\xi$ varies, yet the greater the value of $\xi$, the higher the variation of the compliance. Moreover,

TABLE I
SUMMARY OF THE TIP COMPLIANCE FROM FIG. 8

| | | Configuration 1 | | Configuration 2 | |
|---|---|---|---|---|---|
| | Gain factor | Compliance [mm/g] | Variation ratio | Compliance [mm/g] | Variation ratio |
| Compliance along the $x$-axis | $\chi_x = -1$ | 1.16 | 24.7% | 1.58 | 29.5% |
| | $\chi_x = 0$ | 0.93 | 0% | 1.22 | 0% |
| | $\chi_x = 2$ | 0.75 | -19.4% | 0.96 | -21.3% |
| | $\chi_x = 4$ | 0.62 | -33.3% | 0.78 | -36.1% |
| Compliance along the $y$-axis | $\chi_y = -1$ | 2.61 | 31.8% | 1.83 | 20.4% |
| | $\chi_y = 0$ | 1.98 | 0% | 1.52 | 0% |
| | $\chi_y = 2$ | 1.36 | -31.3% | 1.09 | -28.3% |
| | $\chi_y = 4$ | 0.99 | -49.5% | 0.85 | -44.1% |
| Compliance along the $z$-axis | $\chi_z = -5$ | 0.51 | 34.2% | 0.21 | 23.5% |
| | $\chi_z = 0$ | 0.38 | 0% | 0.17 | 0% |
| | $\chi_z = 5$ | 0.30 | -21.1% | 0.15 | -11.8% |
| | $\chi_z = 10$ | 0.25 | -34.2% | 0.12 | -29.4% |

* The compliance control is not activated when $\chi_x$, $\chi_y$, or $\chi_z$ equals zero, as highlighted in the grey color. The results for softening and stiffening control are coloured in pink and blue, respectively.

the results show that when $\xi = 1$, the compliance is about $2 \sim 3$ times higher than compliance when $\xi = 0.75$, in most cases. Similarly, when $\xi = 0.75$ the compliance is about $2 \sim 3$ times higher than that when $\xi = 0.5$.

*Results for Experiment 4:* Fig. 8(b)–(c) present the compliance response curves along three axes with varying gain factors [see (17)]. Table I provides a summary of identified compliance values and compliance variation ratios defined in (19). The results illustrate that the exhibited robot's tip compliance along three axes is regulated to increase or decrease when the gain factor is smaller (softening control) or lager (stiffening control) than zero, respectively. Fig. 8(b) reports the compliance values along the $x$-axis under two configurations. For instance, the identified compliance in Configuration 1 is 1.16, 0.93, 0.75, and 0.62 mm/g when the gain factor $\chi_x$ is set as –1, 0, 2, and 4, respectively. Compared to the inherent robot's compliance when $\chi_x = 0$, the compliance variation is 24.7%, –19.4%, –33.3% for gain factors of –1, 2, and 4, respectively. In Configuration 2, the compliance variation along the $x$-axis is similar, ranging between –36.1% and 29.5%.

Fig. 8(c) shows the compliance responses along the $y$-axis. In two configurations, the robot's compliance is consistently larger compared to the compliance along the $x$-axis for the same gain value. For instance, in Configuration 1 and Configuration 2, the compliance ranges are [0.99, 2.61] and [0.85, 1.83] mm/g, respectively. The compliance controller varies the robot's compliance along the $y$-axis in the range of –49.5%∼31.8% across the two configurations. Fig. 8(d) illustrates lower compliance responses (e.g., less than 0.51 mm/g) along the $z$-axis in two configurations compared to results from Fig. 8(c)–(d). When the gain factor ranges between –5 and 10, the compliance variation falls within –34.2%∼34.2%.

Fig. 9 further reports the compliance control results when the soft robot interacts with human. The gain factor $\chi_y$ is set as 3. In stage 1, the robot is actuated to Configuration 1, with no interaction between the robot and the finger tip. In stage 2, a tip force $\Delta F$ is applied along the $y$-axis. When the resultant $\Delta y$ reaches 13.9 mm, the pressure from the compliance controller varies from [0.10, 0.53, 0.60] bar to [0.42, 0.87, 0.65] bar. In stage 3, $\Delta F$ is along the $z$-axis. The resulting maximum variation of the pressure vector is [0.03, 0.01, 0.10] bar. In all cases, the maximum deflection values are lower than 20 mm, with $\Delta x$, $\Delta y$, and $\Delta z$ of 15.2, 14.3, and –16.6 mm, respectively.

*Results for Experiment 5:* Fig. 10(b) reports the averaged maximum interact forces before objects are dropped. Without the compliance control, forces are 0.30 N, 0.27 N, and 0.37 N when grasping a strawberry, raspberry and cherry, respectively. In contrast, these forces increase to 0.48 N, 0.47 N, and 0.65 N when the compliance control is deployed. Fig. 10(c) reports the force and control pressure in one trial. In the initial grasping state, the pressure remains constant. During 6∼16 s, forces up to 0.6 N are applied to the object, the compliance controller varies the pressure to stabilise the grasping, as highlighted in the green area. After 16 s, the object drops and the control pressure returns to the initial states.

## IV. DISCUSSION OF VALIDATION RESULTS

Fig. 1 shows the material modulus varies with the strain, and our method accommodates this by calculating the tangent modulus $E$ through differentiating the analytical stress–strain function established from the neo-Hookean model. Fig. 5(a) suggests the $E_l$ is smaller than the real modulus when the stretch ratio $\lambda_1$ is up to 1.5. This explains that the predicted values of the elongation and bending angle from the linear model are larger compared to the experimental values, as demonstrated in Fig. 5(b)–(d). In contrast, the neo-Hookean model performs better within this stretch range. It is noteworthy that linearized model might be considered subjected to a small strain assumption. In our case, it is found that when the maximum stretch is up to 1.3, the identified neo-Hookean model can be linearly fitted using a modulus of 106 kPa, with a coefficient of determination $R^2$ of 0.9957. As such, it is advisable to use the neo-Hookean model when the stretch ratio is over 1.3. In addition, Experiment 1 indicates the elongation and bending responses are flattened, specifically when the stretch ratio is larger than 1.5 or the bending angle is larger than 130° (see Fig. 5). This discrepancy may come from two facts. First, elastomers can exhibit a strain-stiffening when the stress becomes high [40]. Second, the pressurized chambers might increase the flexural stiffness of soft robots [7]. Typically, our static modeling approach for fiber-reinforced soft robots achieves an average position error of 3.4% of the original length of the robot, outperforming the 5% in [15], 6% in [41], and 8% in [16].

10% errors of compliance modeling in Experiment 3 mainly come from two aspects: error propagation from the kinematics model and experimental measurement. Fig. 7 reports that the predicted compliance is smaller than the experimental compliance when the pressure is between $0.9 \sim 1.2$ bar, as bending angles from the simulations are smaller than the experiments [see Fig. 5(c)]. Theoretically, the predicted displacement derived by compliance matrix from (13) satisfies under the small deflection assumption [24]. As a result, the pulling displacement could impact the measured compliance.

TABLE II
COMPARISON BETWEEN OUR VARIABLE COMPLIANCE MODELING AND CONTROL TECHNIQUE AND EXISTING WORKS FOR CONTINUUM ROBOTS

| Reference | Actuation | Compliance-varying Principle | Extra Stiffening Structure | Compliance Modelling Approach | Compliance Modelling Accuracy | Compliance Model-based Control | Considering Hyper-elasticity |
|---|---|---|---|---|---|---|---|
| [4] | Tendon | Tendon tension | No | — | — | No | No |
| [5] | Tendon | Robot length and LMPA | Yes | Model and learning | Not evaluated | Yes | No |
| [7] | Tendon | Pressure stiffening | Yes | Jacobian projection | Not evaluated | Yes | No |
| [8] | Concentric tube | Tube length control | No | — | — | No | No |
| [33] | Pneumatics | Antagonistic actuation | No | Jacobian projection | Not evaluated | No | No |
| [34] | Parallel tube | Tube length control | No | — | — | No | No |
| Our work | Pneumatics | Pressure control | No | Analytical integration | 10% | Yes | Yes |

Moreover, Experiment 4 highlights the effectiveness of the compliance modeling approach in achieving active compliance regulation. By setting positive or negative gain factors in (17), the robot's compliance along the $x$-, $y$-, and $z$-axes can be selectively decreased or increased. The results indicate that large gain factors are required when regulating the robot's compliance along the $z$-axis. This is attributed to the inherent higher compliance values in the $z$-axis compared to compliance along the $x$- and $y$-axes (refer to Fig. 7). It is important to note that the gain factors represent the control efforts exerted by the compliance controller to regulate the robot's compliance when the measured position $p_m$ deviates from the reference position $p_r$. Fig. 9 illustrates that the pressure variation in stage 2 is larger than values in stage 3, and the values of $\Delta x$ and $\Delta z$ result in negligible pressure variations. This indicates that only the compliance along the $y$-axis is under control when $\chi_y$ is set as 3, and the compliance along the $x$- and $z$-axes is not impacted. Experiment 4 employs loads via known weights when validating the compliance controller. Furthermore, the Supplementary Video demonstrating the potential of the proposed compliance regulation approach when the soft robot interacts with a moving contact. Experiment 5 demonstrates that the developed model-based compliance controller improves the grasping ability of soft grippers when exposed to external disturbances. Notably, with compliance control, forces required to cause the release of grasped objects are 60%∼75% higher compared to scenarios without compliance control.

Table II further highlights our contribution to the compliance modeling and control techniques for soft robots. Notably, our work effectively models the compliance of soft robots incorporating material hyperelasticity. Furthermore, our validated compliance model offers a method for achieving model-based compliance regulation without the need for additional stiffening mechanisms [7]. In particular, as highlighted in [8], determining the tip position of a deflected robot requires an additional loop to resolve the forward kinematics under tip loads. In contrast, the tip position of deflected robot in this work (see Fig. 3) is calculated from the modeled compliance matrix (see Section II-C) directly. Importantly, this proposed approach has the potential to be applied to other compliant robots that can be described using Cosserat rod models, such as tendon-driven or parallel continuum robots [8], [20], [37].

## V. CONCLUSION

This article presented a static compliance modeling and control method for pneumatic-driven, hyperelastic soft robots. The material nonlinearity is captured using the neo-Hookean model. The modeled compliance can be utilized to regulate the exhibited robot's compliance in Cartesian space. Simulations and experiments were both conducted for validation. Results demonstrated a high fidelity of the configuration-dependent compliance model, e.g., the average tip position errors and the dimensionless compliance errors are less than 2.03 mm (i.e., 3.4% of the robot length) and 10%, respectively. Moreover, experiments indicated the exhibited tip compliance can be regulated to be lower (–10%∼–50%) or higher (20%∼35%) compared to the inherent robot's compliance. In real-world application, we demonstrated that the proposed compliance control approach enhances the grasping ability of soft grippers.

In future work, we will extend this work to achieve on-demand stiffness/compliance and force control for multisegment robots in more complex scenarios. For instance, it is also interesting to implement our compliance modeling and control approach to scenarios involving the interaction of soft robots with compliant environments. In addition, to capture the strain-stiffening effect, we will also explore to implement high-order hyperelastic models within the proposed approach, e.g., the Mooney–Rivlin, Gent or Yeoh models, and study their influences on the modeling and control accuracy.

## ACKNOWLEDGMENT



## REFERENCES

[1] C. Laschi, B. Mazzolai, and M. Cianchetti, "Soft robotics: Technologies and systems pushing the boundaries of robot abilities," *Sci. Robot.*, vol. 1, no. 1, 2016, Art. no. eaah3690.
[2] L.-J. Gai, J. Huang, and X. Zong, "Stiffness-tunable soft bellows actuators by cross-fiber jamming effect for robust grasping," *IEEE/ASME Trans. Mechatron.*, vol. 28, no. 5, pp. 2897–2907, Oct. 2023.
[3] Y. Cui et al., "Design and implementation of an underactuated gripper with enhanced shape adaptability and lateral stiffness through semi-active multi-degree-of-freedom endoskeletons," *Int. J. Robot. Res.*, vol. 43, no. 6, pp. 873–896, 2024.
[4] J. Lai, B. Lu, and H. K. Chu, "Variable-stiffness control of a dual-segment soft robot using depth vision," *IEEE/ASME Trans. Mechatron.*, vol. 27, no. 2, pp. 1034–1045, Apr. 2022.
[5] J. Zhang et al., "Design and stiffness control of a variable-length continuum robot for endoscopic surgery," *IEEE Trans. Automat. Sci. Eng.*, vol. 22, pp. 5251–5261, 2025.
[6] J. Peters et al., "Actuation and stiffening in fluid-driven soft robots using low-melting-point material," in *Proc. IEEE/RSJ Int. Conf. Intell. Robots Syst.*, 2019, pp. 4692–4698.

[7] F. Stella, J. Hughes, D. Rus, and C. Della Santina, "Prescribing Cartesian stiffness of soft robots by co-optimization of shape and segment-level stiffness," *Soft Robot.*, vol. 10, no. 4, pp. 701–712, 2023.
[8] M. Mahvash and P. E. Dupont, "Stiffness control of surgical continuum manipulators," *IEEE Trans. Robot.*, vol. 27, no. 2, pp. 334–345, Apr. 2011.
[9] L. Marechal, P. Balland, L. Lindenroth, F. Petrou, C. Kontovounisios, and F. Bello, "Toward a common framework and database of materials for soft robotics," *Soft Robot.*, vol. 8, no. 3, pp. 284–297, 2021.
[10] J. Shi, W. Gaozhang, and H. A. Wurdemann, "Design and characterisation of cross-sectional geometries for soft robotic manipulators with fibre-reinforced chambers," in *Proc. IEEE 5th Int. Conf. Soft Robot.*, 2022, pp. 125–131.
[11] A. Stilli, E. Kolokotronis, J. Fras, A. Ataka, K. Althoefer, and H. A. Wurdemann, "Static kinematics for an antagonistically actuated robot based on a beam-mechanics-based model," in *Proc. IEEE/RSJ Int. Conf. Intell. Robots Syst.*, 2018, pp. 6959–6964.
[12] L. Lindenroth, D. Stoyanov, K. Rhode, and H. Liu, "Toward intrinsic force sensing and control in parallel soft robots," *IEEE/ASME Trans. Mechatron.*, vol. 28, no. 1, pp. 80–91, Feb. 2023.
[13] P. Polygerinos et al., "Modeling of soft fiber-reinforced bending actuators," *IEEE Trans. Robot.*, vol. 31, no. 3, pp. 778–789, Jun. 2015.
[14] M. T. Chikhaoui, S. Lilge, S. Kleinschmidt, and J. Burgner-Kahrs, "Comparison of modeling approaches for a tendon actuated continuum robot with three extensible segments," *IEEE Trans. Robot. Automat.*, vol. 4, no. 2, pp. 989–996, Apr. 2019.
[15] D. Trivedi, A. Lotfi, and C. D. Rahn, "Geometrically exact models for soft robotic manipulators," *IEEE Trans. Robot.*, vol. 24, no. 4, pp. 773–780, Aug. 2008.
[16] S. R. Eugster, J. Harsch, M. Bartholdt, M. Herrmann, M. Wiese, and G. Capobianco, "Soft pneumatic actuator model based on a pressure-dependent spatial nonlinear rod theory," *IEEE Trans. Robot. Automat. Lett.*, vol. 7, no. 2, pp. 2471–2478, Apr. 2022.
[17] J. Shi, S.-A. Guaman, J. Dai, and H. A. Wurdemann, "Position and orientation control for hyperelastic multisegment continuum robots," *IEEE/ASME Trans. Mechatron.*, vol. 29, no. 2, pp. 995–1006, Apr. 2024.
[18] Y. Elsayed et al., "Finite element analysis and design optimization of a pneumatically actuating silicone module for robotic surgery applications," *Soft Robot.*, vol. 1, no. 4, pp. 255–262, 2014.
[19] D. C. Rucker and R. J. Webster, "Computing Jacobians and compliance matrices for externally loaded continuum robots," in *Proc. IEEE Int. Conf. Robot. Automat.*, 2011, pp. 945–950.
[20] C. B. Black, J. Till, and D. C. Rucker, "Parallel continuum robots: Modeling, analysis, and actuation-based force sensing," *IEEE Trans. Robot.*, vol. 34, no. 1, pp. 29–47, Feb. 2018.
[21] K. Oliver-Butler, J. Till, and C. Rucker, "Continuum robot stiffness under external loads and prescribed tendon displacements," *IEEE Trans. Robot.*, vol. 35, no. 2, pp. 403–419, Apr. 2019.
[22] C. Della Santina, C. Duriez, and D. Rus, "Model-based control of soft robots: A survey of the State of the Art and open challenges," *IEEE Control Syst. Mag.*, vol. 43, no. 3, pp. 30–65, Jun. 2023.
[23] J. Shi et al., "Screw theory-based stiffness analysis for a fluidic-driven soft robotic manipulator," in *Proc. IEEE Int. Conf. Robot. Automat.*, 2021, pp. 11938–11944.
[24] J. Shi et al., "Stiffness modelling and analysis of soft fluidic-driven robots using Lie theory," *Int. J. Robot. Res.*, vol. 43, no. 3, pp. 354–384, 2024.
[25] A. L. Orekhov and N. Simaan, "Solving Cosserat rod models via collocation and the magnus expansion," in *Proc. IEEE/RSJ Int. Conf. Intell. Robots Syst.*, 2020, pp. 8653–8660.
[26] F. Boyer, V. Lebastard, F. Candelier, F. Renda, and M. Alamir, "Statics and dynamics of continuum robots based on Cosserat rods and optimal control theories," *IEEE Trans. Robot.*, vol. 39, no. 2, pp. 1544–1562, Apr. 2023.
[27] M. Tummers, V. Lebastard, F. Boyer, J. Troccaz, B. Rosa, and M. T. Chikhaoui, "Cosserat rod modeling of continuum robots from Newtonian and Lagrangian perspectives," *IEEE Trans. Robot.*, vol. 39, no. 3, pp. 2360–2378, Jun. 2023.
[28] M. Manti, V. Cacucciolo, and M. Cianchetti, "Stiffening in soft robotics: A review of the state of the art," *IEEE Robot. Automat. Mag.*, vol. 23, no. 3, pp. 93–106, Sep. 2016.
[29] S. G. Fitzgerald, G. W. Delaney, and D. Howard, "A review of jamming actuation in soft robotics," *Actuators*, vol. 9, no. 4, 2020, Art. no. 104.
[30] A. Shiva et al., "Tendon-based stiffening for a pneumatically actuated soft manipulator," *IEEE Trans. Robot. Automat.*, vol. 1, no. 2, pp. 632–637, Jul. 2016.
[31] C. M. Best, L. Rupert, and M. D. Killpack, "Comparing model-based control methods for simultaneous stiffness and position control of inflatable soft robots," *Int. J. Robot. Res.*, vol. 40, no. 1, pp. 470–493, 2021.
[32] W. Gaozhang et al., "A novel stiffness-controllable joint using antagonistic actuation principles," *Mech. Mach. Theory*, vol. 196, 2024, Art. no. 105614.
[33] D. Bruder, M. A. Graule, C. B. Teeple, and R. J. Wood, "Increasing the payload capacity of soft robot arms by localized stiffening," *Sci. Robot.*, vol. 8, no. 81, 2023, Art. no. eadf9001.
[34] V. Aloi, C. Black, and C. Rucker, "Stiffness control of parallel continuum robots," in *Proc. Dyn. Syst. Control Conf.*, 2018, Art. no. V001T04A012.
[35] J. Burgner-Kahrs, D. C. Rucker, and H. Choset, "Continuum robots for medical applications: A survey," *IEEE Trans. Robot.*, vol. 31, no. 6, pp. 1261–1280, Dec. 2015.
[36] H. Abidi et al., "Highly dexterous 2-module soft robot for intra-organ navigation in minimally invasive surgery," *Int. J. Med. Robot. Comput. Assist. Surg.*, vol. 14, no. 1, 2018, Art. no. e1875.
[37] J. Till, V. Aloi, and C. Rucker, "Real-time dynamics of soft and continuum robots based on Cosserat rod models," *Int. J. Robot. Res.*, vol. 38, no. 6, pp. 723–746, 2019.
[38] J. R. Dormand and P. J. Prince, "A family of embedded Runge-Kutta formulae," *J. Comput. Appl. Math.*, vol. 6, no. 1, pp. 19–26, 1980.
[39] J. Shi, W. Gaozhang, H. Jin, G. Shi, and H. A. Wurdemann, "Characterisation and control platform for pneumatically driven soft robots: Design and applications," in *Proc. IEEE Int. Conf. Soft Robot.*, 2023, pp. 1–8.
[40] C. O. Horgan, "The remarkable gent constitutive model for hyperelastic materials," *Int. J. Non-Linear Mech.*, vol. 68, pp. 9–16, 2015.
[41] S. M. H. Sadati, S. E. Naghibi, I. D. Walker, K. Althoefer, and T. Nanayakkara, "Control space reduction and real-time accurate modeling of continuum manipulators using Ritz and Ritz–Galerkin methods," *IEEE Trans. Robot. Automat.*, vol. 3, no. 1, pp. 328–335, Jan. 2018.

**Jialei Shi** received the B.S. degree in naval architecture and ocean engineering from the Harbin Institute of Technology, Harbin, China, in 2017, the M.S. degree in aerospace engineering from the Beijing Institute of Technology, Beijing, China, in 2019, and the Ph.D. degree in mechatronic and robotic engineering from the University College London, London, U.K., in 2024.

He is currently a Research Associate with Hamlyn Centre, Imperial College London, London, U.K. His research interests include design, modeling, and control of soft robotics and medical devices.

**Sara-Adela Abad** (Member, IEEE) received the B.Eng. degree in electronic and control engineering from National Polytechnic School, Quito, Ecuador, in 2010, the M.Sc. degree in AI from the University of Southampton, Southampton, U.K., in 2013, and the Ph.D. degree in robotics from Imperial College London, London, U.K., in 2019.

She is currently a Lecturer in robotics with Mechanical Engineering Department, University College London, London, U.K. Her research interests include bioinspiration, adaptability to uncertain conditions, and compliant robotics.

**Ge Shi** (Member, IEEE) received the B.S. degree in electrical and electronic engineering from the University of Strathclyde, Glasgow, U.K., in 2016, and the M.S. degree in power system engineering and the Ph.D. degree in mechanical engineering from University College London, London, U.K., in 2017 and 2023, respectively.

His research interests include haptic feedback systems, soft robotics, and medical devices.

**Wenlong Gaozhang** (Student Member, IEEE) received the B.S. degree from Xiamen University, Xiamen, China, in 2017, and the M.S. degree from Xi'an Jiaotong University, Xi'an, China, in 2020, both in mechanical engineering. He is currently working toward the Ph.D. degree in mechanical engineering with University College London, London, U.K.

His research interests include soft robotics and collaborative robots.

**Jian Sheng Dai** (Fellow, IEEE) received the Ph.D. degree in advanced kinematics and robotics from the University of Salford, Salford, U.K., in 1993.

He has authored or coauthored more than 500 publications. His research interests include mechanisms and robotics with focus on kinematics, screw theory, metamorphic mechanisms, reconfigurable mechanisms and robotics.

Dr. Dai is Fellow of the Royal Academy of Engineering, Member of Academia Europaea. He was presented with the ASME Machine Design Award as the 58th recipient since the inception of the Award in 1958.

**Helge A. Wurdemann** (Member, IEEE) received the Dipl.-Ing. degree in electrical engineering with a focus on mechatronics and robotics in the medical field from the Leibniz University of Hanover, Hanover, Germany, in 2008, and the Ph.D. degree in robotics from King's College London, London, U.K., in 2012.

He is currently a Professor of robotics with University College London, London, U.K., leading robotics in the Department of Mechanical Engineering. He has authored more than 100 articles, published in high-impact journals, and peer-reviewed full-length conference papers.